Investigation of models to estimate flight performance of gliding birds from wakes

Jialei Song[1,3*], Changyao Chen[1], Jorn A. Cheney[2], James R. Usherwood[3], Richard J. Bomphrey[3]

[1] School of Mechanical Engineering, Dongguan University of Technology, Dongguan, Guangdong, China

[2] School of Biological Sciences, University of Southampton, Southampton, SO17 1BJ, UK

[3] Structure and Motion Laboratory, Department of Comparative Biomedical Sciences, Royal Veterinary College, North Mymms, Hatfield AL9 7TA, UK

* Author to whom any correspondence should be addressed.

Email: songjl@dgut.edu.cn

Abstract

Mathematical models based on inviscid flow theory are effective at predicting the aerodynamic forces on large-scale aircraft. Avian flight, however, is characterized by smaller sizes, slower speeds and increased influence of viscous effects associated with lower Reynolds numbers. Therefore, inviscid mathematical models of avian flight should be used with caution. The assumptions used in such models, such as thin wings and streamlined bodies, may be violated by birds, potentially introducing additional error. To investigate the applicability of existing models to calculating aerodynamic performance of bird flight, we compared predictions using simulated wakes with those calculated directly from forces on bird surface, both derived from computational fluid dynamics (CFD) of a high-fidelity barn owl geometry in free gliding flight. Two lift models and two drag models are assessed. We show that the generalized Kutta-Joukowski model, corrected by the streamwise velocity, can predict not only the lift but also span loading well. Drag was predicted best by a drag model based on the conservation of fluid momentum in a control volume. Finally, we estimated force production for three raptor species across nine gliding flights by applying the best lift model to wake flow fields measured with particle tracking velocimetry (PTV).

Keywords: bird flight, theoretical aerodynamic models, lift and drag, flow visualization

1. INTRODUCTION

The aerodynamic performance of gliding birds raises questions for biologists and aeronautical engineers: how economical are birds, and how is this economy achieved? To approach these questions and understand their implications, reliable aerodynamic measurements and models are required. Various methods have been adopted for approaching such questions, ranging from simple analytical models based on theory developed for aircraft to, increasingly, those leveraging advances in imaging (of bird surfaces and wakes) and computer power (allowing computational fluid dynamics)[1-3]. Empirical methods for determining lift, drag and span efficiency exploit advanced quantitative measurements of wakes using particle image velocimetry (PIV) or particle tracking

velocimetry (PTV); however, these rely on advanced aerodynamic theory and various assumptions for such parameters to be deciphered[4-7]. Several models have been proposed to estimate the lift using the wake behind birds, using either conventional aerofoil theory or, more fundamentally, the conservation of momentum[8, 9]. According to the Kutta-Joukowski theorem, lift per span can be estimated by calculating the bound circulation on the wing chord. As Kelvin's theorem shows that the strength of circulation along the enclosed circle is an invariant for potential inviscid barotropic flow (a widely used assumption for bird flight), the bound circulation can be predicted from the vortex distribution behind the trailing edge, which makes it possible to measure the spanwise lift distribution on the assumption of negligible spanwise flow. Using the principle of fluid momentum conservation, van Dam *et al.* derived a model that estimates lift by analyzing the wake within an infinitely large plane which is parallel to the frontal plane[10, 11]. Despite this approach could accurately predict the lift of a flying jackdaw[12] and similar approaches have accurately predicted the lift of flying swifts and moths[5, 6], the reliability still requires validation due to the fact that lift estimates from wake measurements are sensitive to the downstream location of the measurement plane as well as the line to sample the downwash[13-15], making it challenging to use the rightful wake information.

Besides the lift, drag can also be estimated by the wakes. A widely used drag model decomposes drag into three components[16] : profile drag $D_{pro,}$ parasite drag D_{par}, and induced drag D_{ind}. The profile drag contains a component of skin friction and the pressure difference between frontal and rear surfaces of the wings, while parasite drag is determined by the shape of the body and tail. Both of them are proportional to the product of air density ρ, the square of velocity U_{∞}, and their respective characteristic areas, with D_{pro} proportional to planform area S and D_{par} to frontal area S_A. The corresponding coefficients are labeled as profile drag coefficient $C_{D,pro}$ and parasite drag coefficient $C_{D,par,}$ both of which can be estimated from the wakes. Previously, in the absence of a better estimate in the biological literature, the profile drag coefficient has often been treated as a constant for individual birds; for example, 0.0207 ± 0.0079, was obtained when measuring a flying hawk with Reynolds number in the range $1.43\text{-}1.94 \times 10^5$[17]. Whereas, later studies showed profile drag coefficient varies with Reynolds number[7] and is a function of lift coefficient as well[18], indicating that a constant profile drag coefficient may be inappropriate. Parasite drag can be calculated using the streamwise momentum loss caused by the body/tail [19, 20], allowing for the determination of the parasite drag coefficient. However, this calculation faces challenges due to the variation in configuration between flights, which may be correlated with flight speed, and the bird's instantaneous configuration[5, 21, 22]. The third component, induced drag, labelled as D_{ind}, arises when the lifting surface produces lift, redirecting the flow downward, given by

$$D_{ind} = \frac{2kL^2}{\pi\rho b^2 U_{\infty}^2} \qquad (1)$$

where b is wing span, and k is the inverse of the span efficiency factor related to the spanwise loading distribution's deviation from an elliptical profile. Often, k has been set to 1.1-1.2 for

reasonably efficient wing designs in real birds[23]. In contrast, values of k for insects (*e.g.* locusts or hawkmoths) can be higher: from 1.12 to 1.88[4, 15, 24]. However, selecting the appropriate value of k for accurately estimating induced drag presents its own challenges. The value of k changes with the Reynolds number and is particularly crucial at the low and moderate Reynolds numbers encountered in bird flight[25]. This necessitates considerable caution when applying a constant or assumed 'k' factor in the context of bird flight. In lifting-line theory, induced drag is calculated based on the spanwise downwash profile induced by the shed vortex[26]. However, the downwash exhibits significant variation across various downstream planes (with normal vectors parallel to the incoming flow)[4, 16], thereby complicating the determination of induced drag. This complexity arises because the induced drag is dramatically affected by the differences in the sampled downwash region[4, 16]. An alternative method directly estimates induced drag using the vertical velocity (downwash) and transverse velocity on a sampling plane[11, 27, 28]. This approach necessitates a large and distant sampling plane from the flying bird to fulfill the model's assumptions[34].

In this paper, we develop a computational fluid dynamics (CFD) model, with a high-fidelity surface derived from photogrammetry, for a gliding barn owl, *Tyto alba*, to obtain force estimates from the bird surface and the surrounding flows. We then compare these body-derived forces with those from theoretical wake-based models to assess model performance, by considering the effect of sampling planes. The most accurate model is subsequently applied to analyze the wake of three raptor species (barn owl (*Tyto alba*), tawny owl (*Strix aluco*) and goshawk (*Accipiter gentilis*)). The wakes of these species were measured by large-volume, high-resolution particle tracking velocimetry (PTV). This exploration aims to validate a range of commonly used theoretical models and refine theoretical force models to improve the estimation of flight performance in flying animals based on wake measurement, where highly controlled – and so inevitably highly constrained – measurements are not practicable.

2. MATERIALS AND METHODS

2.1. Mathematical model

In this study, the laboratory coordinate system $oxyz$ is set in the following way: the origin of the coordinate system locates at the sagittal plane: x directs downstream, y directs laterally and z directs upward, as shown in Figure 1(a).

2.1.1. Lift models

According to Kelvin's theorem, bound circulation on the wing chord can be estimated from the wake behind the trailing edge. The wake shed from the wing is assumed to be a continuous vortex sheet extending downstream from the trailing edge (Figure 1(a)). Consequently, the correlation between bound circulation and downstream wake can be expressed as follows:

$$\begin{cases} \frac{d\Gamma_y}{dy} = \int_{-\infty}^{+\infty} \omega_x \, dz = \eta(y); \\ \Gamma_y(y = \pm b/2) = 0 \end{cases} \quad (2)$$

where Γ_y is the bound circulation, $\eta(y)$ represents the specific circulation on the wing chord, and b is the span length. ω_x is the streamwise vorticity obtained on the sample cross-stream plane, which is parallel to the *yoz* plane. The lift per span is calculated as follows:

$$\tilde{L}_y = \rho U_\infty \Gamma_y \quad (3)$$

where ρ is air density, the lift per span $\tilde{L}$ is perpendicular to the incoming flow velocity U_∞ and the drag per span $\tilde{D}_y$ is zero under the potential flow assumption. This lift model is henceforth referred as KJC. In the case of 3D wings, interactions occur among chord sections, largely culminating in a combined vortex at each wing tip with opposing-sign circulation[29, 30]. Consequently, modifications are required both in the estimation of sectional lift and drag. In reality, the generated lift aligns not perpendicular to the incoming flow U_∞, but rather perpendicular to the local velocity U_r'. This local velocity includes the resultant downwash, w', which is opposite to the rotated lift direction, as shown in Figure 1(b), which is adapted from Usherwood and Ellington[31]. A model that considers variation along the wing span should use the induced local velocity rather than U_∞:

$$\tilde{L}_y = \rho U_r' \Gamma_y \quad (4)$$

where U_r' is the effective streamwise velocity, and w' is the induced downwash. In Eq. 4, U_r' is the effectively incoming flow velocity, which is described in Figure 1(b). U_r' is calculated as $U_\infty cos\alpha_p$, where $\alpha_p = \cos^{-1}(w'/U_\infty)$, and $w' = U_r' \tan\alpha_p$. Theoretically, the determination of U_r' is an iterative process. As the downwash is small, we ignored the iterative process and the downwash $w' = w\cos(\tan^{-1}(w/U_\infty))$ in this model and $U_r' = U_\infty \cos(\tan^{-1}(w/U_\infty))$. The value of w is obtained on the horizontal transects of transverse planes after passage of the bird, located level with the wingtips. Meanwhile, the induced drag per span $\tilde{D}_y$ can be estimated as $\rho w' \Gamma_y$. Substituting Eq. 2 into Eq. 4 yields the force model based on the generalized Kutta-Joukowski theorem. This lift model is henceforth referred as KJG.

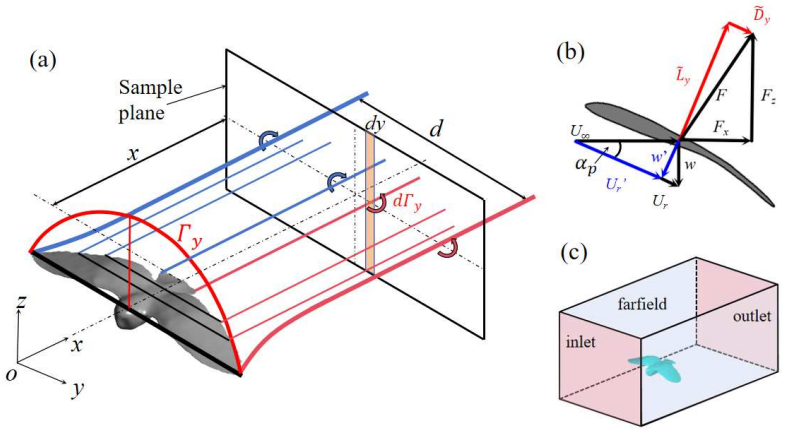

Figure 1: (a) Illustration of the span loading estimation of a bird using Kelvin's theorem and the vortex filament model. In this model, vortices shed along the span continuously, causing the change in bound circulation Γ_y. (b) Illustration of the flow velocities and corresponding forces. *Ur'* and *w'* in blue refer to the parameters used in the Kutta-Joukowski generalized model. (c) Illustration of the surface of control volume for drag calculation using the wake (not to scale).

Due to the pressure difference between the wing's lower and upper surfaces at the wing tips, the wing tip vortices are formed, associated with downward flow between the two cores and upward flow outside them. The downwash occurring between the cores of the wing tip vortices can be used for force estimation. Please note that the distance between these two wing-tip cores varies slightly due to the contraction of the two (near-) parallel contra-rotating trailing vortices; the distance is defined as the 'pseudo wingspan', *d*, which is a crucial parameter for force estimation[32]. Meanwhile, the distance of non-zero specific circulation $\eta(y)$ is labeled as *b'*, which equals to 'pseudo span' *d* plus the radii of left/right wing tip vortex. Span loading is predicted by scaling both the lateral distribution of incoming flow velocity and downstream circulation distribution to the physical wing span *b*, which is given by:

$$\tilde{L}_y(y) = \rho U_r'(\frac{yd}{b}) \int_y^{b/2} \eta(\frac{yb'}{b}) dy \qquad (5)$$

Then the overall lift of the bird, denoted as *L*, is obtained by integrating the lift per span in Eq. 5:

$$L = \int_{-b/2}^{b/2} \tilde{L}_y(y) dy \qquad (6)$$

2.1.2. Drag models

As the drag exerted on the bird has a reaction force on the fluid, the drag can be estimated by analyzing the variation of fluid velocity and applying the principle of momentum conservation [11]. The control volume of the fluid and the body is enclosed by external surfaces S_e, which includes the inlet surface S_{inlet}, outlet surface S_{outlet} and farfield boundaries $S_{farfield}$ (shown in Figure 1(c)). As the

velocity on the farfield boundaries and inlet are same as incoming flow velocity U_∞, the drag D can be calculated:

$$D = 0.5\rho \iint_{S_e} (v^2 + w^2 + {U_\infty}^2 - u^2)\, dS \qquad (7)$$

Usually, the velocity components, u, v and w, are measured on planes perpendicular to the freestream flow, *i.e.*, the inlet and outlet planes, rather than the enclosed surface enveloping the bird. Additionally, the velocity on the inlet plane and the side farfield planes equals U_∞, cancelling the contributions of these planes. This simplifies Eq. 7 to become:

$$D = 0.5\rho \iint_{S_{outlet}} (v^2 + w^2 + {U_\infty}^2 - u^2)\, dS \qquad (8)$$

When using this equation, it is important that the downstream sampling planes are sufficiently large to conserve mass and prevent fluid from escaping through the side surfaces of the control volume. This model is referred as CMV1. However, obtaining the flow in a large plane is sometimes impractical, in which case an extra term $\rho(u - U_\infty)^2$ is introduced to amend the mass conservation within the control volume. With this adjustment, overall drag, referred as CMV2, which is given by:

$$D = 0.5\rho \iint_{S_{outlet}} (v^2 + w^2 + 2u(U_\infty - u)\, dS \qquad (9)$$

2.2. Subjects and stereo photogrammetric measurement

The bird model used in our CFD simulations, shown in Figure 2(a), is based on the geometry of a freely gliding, mature, female barn owl (*T. alba*), measured at the Royal Veterinary College (Hatfield, UK). The geometry of the bird was measured by multiple-camera stereo photogrammetric experiments in a 17-m long corridor, where cameras were placed above and below the gliding bird, in order to view the dorsal and ventral surfaces. Previously[33], we created a surface mesh for CFD based on measured point clouds acquired by multi-camera photogrammetry (Photoscan version 1.3.5; Agisoft LLC, St Petersburg, Russia) and custom Python scripting. The reconstructed geometry reflects a glide angle of 2.9°, a flight speed 7.88 m/s, aspect ratio 5.12, average chord length $\bar{c}$ = 0.17 m, planform area 0.148 m^2 and body frontal area 0.01 m^2, with more parameters given in Table 1. It is important to note that, in this study, we do not employ the gliding angle and body weight for drag estimation, as the gliding conditions are not strictly balanced, with the mean forward acceleration 0.21 m/s^2, and drag sensitivity is high due to its relatively small value compared to the weight. All work was approved by the Ethics & Welfare Committee of the Royal Veterinary College (URN 2015 1358) and complied with all relevant ethical regulations.

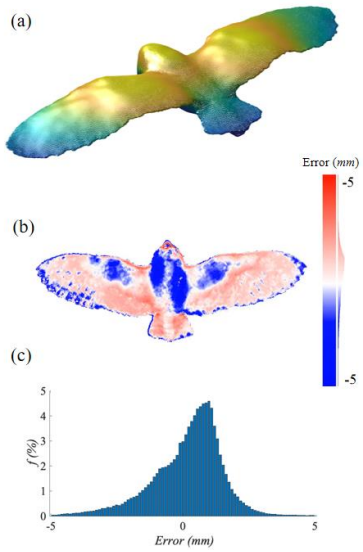

Figure 2: (a) The reconstructed bird surface based on a point cloud from photogrammetric measurements. Very small textural details are excluded; (b) the distance error from the vertices of surface mesh to points cloud and (c) histogram of the distance between the point clouds and the surface mesh reconstructed from the point clouds. 100% of mesh vertices were within 5 mm of the point cloud, 96% within 3 mm and 90% were within 2 mm.

Species	Mass, *M* (g)	Wing span, *b(m)*	Tail span, *bt(m)*	Gliding angle, *θ(degree)*	Speed, *U(m/s)*	W_p
T. alba (CFD)	340	0.87	0.149	2.9	7.88	0.96
T. alba (PTV)	318	0.834	0.138	2.5	7.66	0.89
	318	0.891	0.157	1.1	7.35	1.17
	318	0.850	0.162	3.1	7.52	1.06
S. aluco (PTV)	347	0.829	0.173	6.3	5.86	1.11
	347	0.837	0.211	5.8	5.82	1.17
	347	0.809	0.162	4.6	6.02	1.02
A. gentilis (PTV)	985	1.090	0.395	1.1	7.99	1.05
	985	1.095	0.441	1.1	7.30	1.02
	985	1.011	0.399	0.7	7.91	1.10

Table 1: Summary of parameters and values for and from CFD, and from PTV measurements of three glides of three raptors.

2.3. Particle tracking velocimetry

Particle tracking was conducted separately from the point cloud measurements. In this experiment, we measure the wakes behind three birds: a barn owl, a tawny owl (*Strix aluco*) and a northern goshawk *(Accipiter gentilis)*. During the measurements, 300 μm neutrally-buoyant bubbles filled with a helium-air mixture were used as tracer particles to visualize the wake. Arrays of LEDs were synchronized with the camera shutter, illuminating a volume that was captured using four high-speed cameras recording at 700 Hz (VEO 640L; Phantom Inc. Fastcam SA3; Photron Inc.). The "Shake-the-Box" (STB) algorithm, a 4D particle tracking algorithm that identifies particle

positions in 3D space by triangulation and follows individual particles over time, was used to process the bubble data. The outputs consisted of approximately 20,000 individual particle tracks, from which fluid velocities and accelerations are derived. The wake was measured on the transverse plane locating 0.5 meters behind the tail tip. The detailed information of particle tracking is describe in our previous published paper[34].

2.4. Computational Fluid Dynamics modelling

CFD modelling is used to predict the flow field of the wake and the aerodynamic forces on body and wings in gliding flight, similar to our previous work[35]. Commercial software Mimics (Materialise NV, Leuven, Belgium) and SpaceClaim (version 19.2, ANSYS Inc., Canonsburg, USA) were used to create a high-fidelity surface mesh from a point cloud of the owl in a real glide posture after preprocessing the point clouds. The fluid mesh, created using ANSYS Meshing, encompassed a simulation domain ($53\bar{c} \times 35\bar{c} \times 35\bar{c}$) and consists of approximately 46 million non-uniform volume elements. To accurately resolve the boundary layer near the bird surface, 20 inflation layers were used to resolve the boundary layer: the first layer thickness was δ_t = 0.08 mm (y^+ ~2) and subsequent layers had a growth ratio of 1.2. The simulation setup and the mesh configuration are shown in Figure 3(a) and (b), respectively. Mesh independence is validated and shown in Table 2, supporting the choice of the mesh in this study.

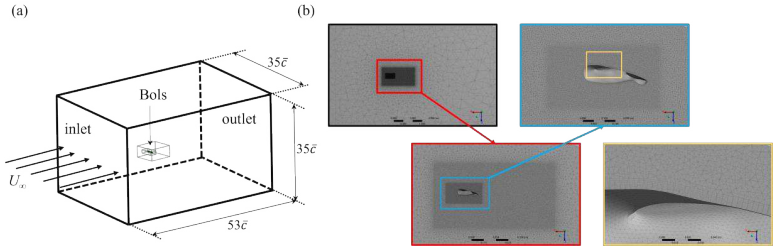

Figure 3: (a) CFD simulation setup and (b) the mesh on the sagittal plane of the computational domain shown at different levels of magnification.

First layer thickness	y^+	Lift (N)	Drag (N)
δ_t = 0.08 mm	~ 2	3.22	0.2834
δ_t = 0.10 mm	~ 3	3.17(1.55%)	0.2827(0.25%)
δ_t = 0.20 mm	~ 7	3.15(2.17%)	0.2925(3.21%)

Table 2: Mesh convergence study. The first layer thickness was changed while the inflation thickness is maintained.

The inlet velocity (U_∞) was set to 7.88 m/s, giving a Reynolds number defined by the average chord length of Re = 88,000; the outlet was set as a Neumann boundary condition. Pressure at the inlet and outlet also followed the Neumann boundary condition. The farfield side boundaries are treated as symmetric, and the turbulence intensity is specified as 1% at the inlet. Ideally, accurately resolving the flow at this Reynolds number requires Direct Numerical Simulation (DNS) with an ultra-dense mesh to capture the Kolmogorov scale, along with extremely fine temporal resolution.

However, this exceeds our computational capabilities. Therefore, to simulate the flow effectively with a feasible grid resolution, we employed the $k-\omega$ SST turbulence model. This model merges the advantages of both the standard $k-\varepsilon$ model and standard $k-\omega$ model, providing a reliable prediction of flow and forces on the bird[35].

We considered the simulation solution to be converged when three, dimensionless, scaled residuals reached a minimum threshold: the continuity residual < 5×10^{-3}; each of the orthogonal velocity component residuals < 5×10^{-7}; and the turbulence kinetic energy < 5×10^{-4}. In general, the turbulence kinetic energy criterion was the last to be met. Residuals were scaled by the maximum residual value among the first five iterations of the simulation. The time step for each simulation is set at Δt = 0.1 ms, corresponding to CFL number = $(u/\Delta x + v/\Delta y + w/\Delta z) \approx 0.40$, meaning that the CFL criterion is met. The detailed validation is described in previous work [35], where we performed a comparison between several turbulence models and our PTV measurements. The outcome was that the *k-ω* model performed best for these Reynolds numbers (88,000).

3. RESULTS AND DISCUSSION

3.1. Tip vortex circulation in CFD

In this study, we firstly focus on wing tip vortices, which are the dominating wake structure for gliding birds, as shown in Figure 4(a). Their strength is indicative of wing's lift and induced drag[8, 9]. We estimate the circulation strength of the tip vortices on the downstream plane in CFD simulations from the surface integration of the *x* component of vorticity ω_x. The center of each tip vortex is located at the point where ω_x reaches its maximum within the vortex. The values of circulation $\Gamma_{wingtip}$ are similar for both wing tip vortices: 0.29±0.003 m^2/s for left, and 0.35± 0.002 m^2/s for right. The variation of $\Gamma_{wingtip}$ is minimal (less than 10%) at different downstream sample planes, with the distance of the sampling plane to the tail tip *x/c* ranging from zero to approximately seven, as shown in Figure 4(b). This small variation of circulation with distance *x/c* suggests that the selection of the plane has limited impact on the calculation of circulation in avian gliding flight. Using the prominent wing tip vortices shed downstream only, without including any other streamwise vorticity, we estimate the lift to be $F = \rho U_\infty \Gamma b$ = 2.68 N, amounting to just 81% of body weight. Including the tail vortices, with values $\Gamma_{tail,left}$ = 0.15 ± 0.003 m^2/s and $\Gamma_{tail,right}$ = 0.22 ±0.003 m^2/s, slightly alters the result, yielding a lift of F = 2.96 N, or 89% of body weight. In comparison, the lift model adopted by Henningsson *et al.*, which used wingtip and tail circulations measured by PIV, predicted lift values varying between 90% to 105% for a common swift (*Apus apus*) at speeds of 7 to 11 ms^{-1}[5]. Presumably the reason for a weight support deficit in our study is the neglected vorticity shed into the wake between the wing tip and wing root on each side. Focusing solely on tip and tail vortices may be inadequate for comprehensive avian aerodynamic analysis, and all the vortices shed behind the bird may need to be taken into account.

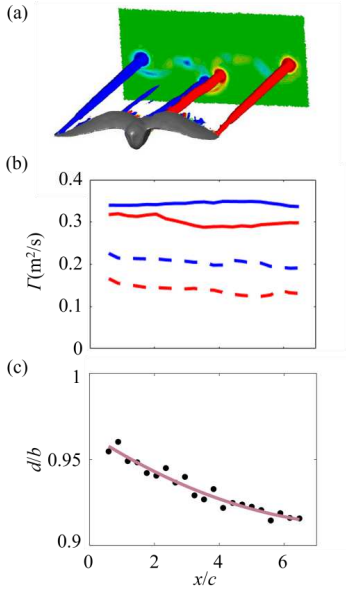

Figure 4: (a) The main vortex structure obtained from CFD simulation. Wingtip vortex and tail vortex are the main structures visible, though smaller structures are apparent. (b) The circulation variation with the distance of sample plane *x/c* of the two wingtip vortices (solid lines) and two tail vortices (dashed lines). (Here red denotes left and blue denotes right). (c) The variation of wing tip vortex distance with the distance of sample plane *x/c* (black dots denotes the original data obtained from CFD, and the solid line denotes the fitted curve).

3.1.1. Evaluation of lift models using CFD

The vortex dynamics influence spanwise distance between two wing tip vortices, making it less than the wingspan. Prior theoretical study has shown that for an elliptically loaded wing, the distance, denoted as d, is $\pi/4$ of wing span[16]. Measurements for a gliding kestrel indicate d to be $0.79b$[32],aligning closely with the theoretical prediction. In this CFD analysis, we observed that d decreases slightly with downstream distance of the measurement plane, and derived values ranging from 0.96 to 0.92 on the plane $x/c = 6$ downstream of the tail (Figure 4(c)). Our study defines 2% of maximal vorticity as the threshold for delineating the vortex outline. As is mentioned above, the distance of non-zero specific circulation is calculated as $b' = d + r_{0,left} + r_{0,right}$, where $r_{0,left}$ and $r_{0,right}$ are the radii of left/right tip vortex. The radii denoted by r_0 are $0.066b$ and $0.073b$ for the left and right wingtips, respectively.

In CFD simulation, lift can be estimated either from the wake on a 2 m × 2.7 m domain using theoretical models and simulated wakes, or directly obtained from the force distribution on bird's surface (Figure 5(a)), the latter of which is labeled as PRS (pressure and viscous stresses on surface). We can compare the lifts obtained in both approaches, with respect to the lift of the integrated bird and the span loading. Figure 5(b) shows the lift estimated using the wake by two models, with the wake sampling on different downstream planes normalized by the lift L_0 from bird body (L_0 account for 96% of the actual weight). Both the KJC and KJG model predict the overall lift from PRS very well, irrespective of downstream distance of the sampling plane within reasonable bounds, with error typically less than 5%. Figure 5(c) illustrates the span loading distributions for KJC and KJG

alongside the PRS. Both the KJC and KJG models accurately predict span loading at the wings. However, near the body and tail, the KJC tends to overestimate loading, whereas KJG model provides a more accurate estimate of loading in this area. At a measurement plane located $x/c = 3.3$ downstream, KJC provides 100.1% of the lift estimated by PRS, while KJG provides 103.0% of the lift estimated by PRS. The KJG model offers superior prediction accuracy on lift with minimal spanwise discrepancy on span loading. As depicted in Figure 5(d), while the rms for the spanwise lift distribution is less than 4.0% for both the KJC and KJG models, the KJG demonstrate a smaller discrepancy.

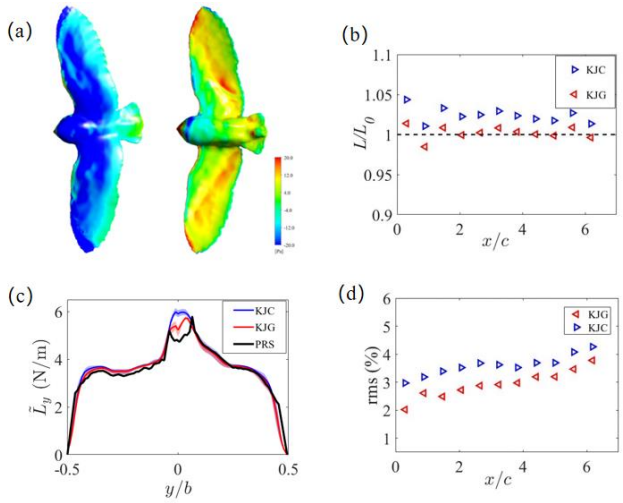

Figure 5: (a) Force per unit area distribution on the surface of a barn owl. (b) Lift comparison between different models. (c) Lift span distribution of KJC and KJG compared with PRS. The shaded areas indicate the values obtained from different sample planes. (d) The rms values of lifts from KJC and KJG with distance between sample planes and body center.

3.1.2. Evaluation of the drag models in CFD

Models to predict the overall drag were based on the conservation of momentum in the streamwise direction. Figure 6(a) shows the overall drag estimation using two drag models on planes at a range of downstream distances from the bird. The CMV1 and CMV2 models returned similar magnitudes, with CMV1 slightly larger than CMV2 in the nearfield wake. At planes located within $x/c < 2$, drag is overestimated by these two models with respect to that from PRS (up to 1.47 at $x/c = 0.89$). However, further downstream ($2.1 \leq x/c \leq 6.2$), drag is slightly underestimated by both models, eventually stabilising at $96 \pm 5\%$. At a measurement plane located $x/c = 3.3$ downstream, CMV1 provides 95.8% of the drag estimated by PRS, while CMV2 provides 94.4% of the drag estimated by PRS.

On the surface of the bird geometry, spanwise flow is generally weak except near the torso,

where the cylindrical shape induces diverging spanwise flow. Therefore, the drag on the wing sections can be predicted by the flow deceleration passing it, and we can produce a spanwise drag distribution. As shown in Figure 6(b), while the drag models can predict the average drag, they differ markedly from the PRS estimate of the spanwise drag distribution. The spanwise drag error is proportionally greatest adjacent to the wingtips and the body/tail. This discrepancy is likely due to strong lateral flows in these two regions caused by deflections of the flow due to the head, or by the wingtip vortices, respectively. For this reason, relying on streamwise loss of momentum may be an inaccurate measure of sectional parasite drag but provides a relatively good average. From CFD analysis, the parasite drag coefficient on the body is $C_{D,par} = 0.31$ (scaled by body frontal area), while CMV1 and CMV2 give $C_{D,par} = 0.26$ and 0.30, respectively. These values align with previous studies using the same drag models to estimate the drag from PIV, which ranges from 0.3 (at 7 ms^{-1}) to 0.22 (at 11 ms^{-1}) for common swift (*Apus apus*)[5] and from 0.6 (at 7 ms^{-1}) to 0.2 (at 11 ms^{-1}) for a jackdaw[19].

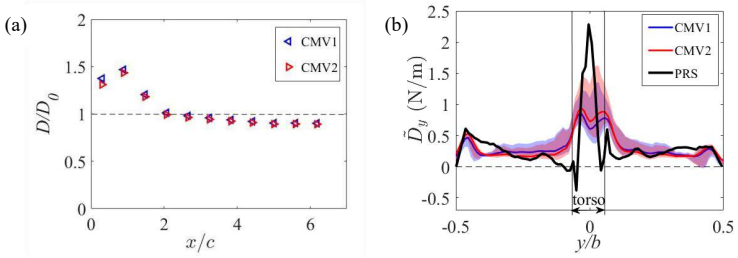

Figure 6: (a) Total drag estimates using two drag models, sampling the wake at different stream-wise planes, normalized by the CFD estimate (PRS). In the near wake, both CMV models over-predict drag with respect to the CFD result but, further back in the wake, they settle to a value close to the CFD prediction with a minor under estimation. (b) Spanwise drag distribution estimates from two drag models and PRS. The shaded areas represent the range of estimates due to different downstream sampling planes.

3.2. Application of the model to a range of tail pitch angles in CFD

The comparison of models, described in the previous section, shows the main discrepancies in span loading estimated by the KJC and KJG models happens at the torso/tail area, and KJG provides a better estimation with respect to CFD (PRS) simulations. As the bird typically pitches down the tail for high angles of attack, and hence high lift [5, 34], we investigated the performance of the models when predicting flight forces with the tail pitched-down. Figure. 7(a)-(d) show the span loading with four different tail pitching angles: $\gamma = -20^o, -10^o, 10^o, 20^o$, deviating from the tail posture originally observed in free gliding experiments where negative 20 degrees (tail depression) means an increased aerodynamic angle of attack. As shown in Fig. 7(e) and 7(f), the KJG model not only estimates total lift more accurately than the KJC model, but also exhibits a smaller discrepancy with PRS across the wingspan.

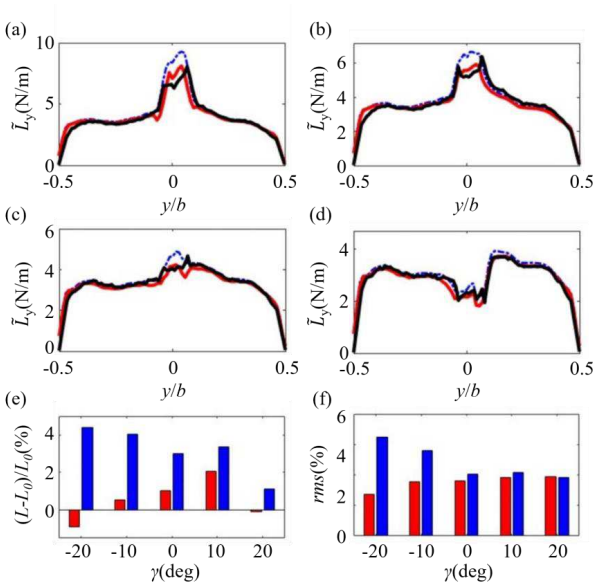

Figure 7: Lift distribution along the wing span using KJC (blue), KJG (red) and PRS (black) with different tail pitch angles. (a) $\gamma = -20^{\circ}$; (b) $\gamma = -10^{\circ}$; (c) $\gamma = 10^{\circ}$; (d) $\gamma = 20^{\circ}$; (e) Lift difference between lift by KJC (blue) and KJG (red) to the lift directly from CFD at different tail pitching angles. (f) lift distribution rms discrepancy with PRS of with KJC (blue) and KJG (red) models, with different tail pitching angles.

3.3. Implementation of models to PTV measurement

The comparison between the models applied to simulated wakes and the PRS results shows that the KJG model predicts lift forces effectively, and the CMV1 model predicts drag forces reasonably accurately for the gliding flight in our birds. However, in previous comparisons, the wake sampling planes were perpendicular to the flying direction, typically achieved in tilted wind-tunnel experiments[17, 20]. In the current study, the wake obtained from our PTV measurements is on vertical plane in a flight corridor[34]. Therefore, while our PTV measurement can be used for lift estimation at low gliding angle, they are unsuitable for drag estimation. Three different bird species flew through the experimental volume, with three measurements processed for each individual. The sampling plane was $x/c = 3.3$. Figure 8 shows streamwise vorticity, ω_x, for the nine gliding flights. Aside from tip and tail vortices, substantial additional vorticity is apparent, which indicates changes in the span loading in the space between the wing tip and tail. Here, because the birds flew at a range of lateral positions across the measurement volume, the PTV visualization sometimes missed part of the span, and, consequently, for six of the nine flights we analysed wakes behind half the wingspan; the complete span loading in those cases is shown by mirroring the half that was analysed. The span loading of the nine flights as estimated by the KJG model is shown in Fig. 9.

The variations of the span loading curves originate from the shed vortices. The sharp increase of loading on wing tip indicates a strong wing tip vortice while the sharp increase on near the edge of torso indicates a strong tail tip vortices (shown on a1, b2, b3 in Figure 9). Meanwhile, the decrease of loading from wing tip to torso indicates the vortex rotating in opposite direction with the wing tip vortex on the same side, as is shown on second flight of the barn owl (a2 in Figure 9). This flight also has the highest wing loading. W_p is the ratio between the overall lift and the normal component of bird weight $Mgcos\theta$. Each measurement has W_p close to 1 (see Table 1). This indicates that the KJG lift model can accurately predict the overall lift as well as the span loading.

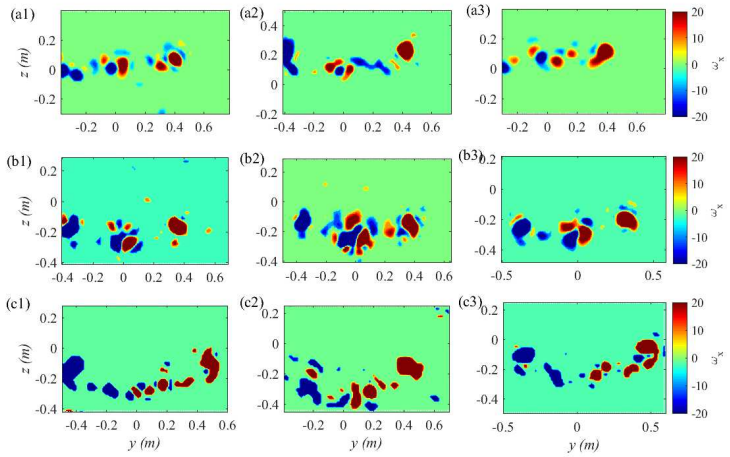

Figure 8: (a) Streamwise vorticity, ω_x, of three raptors. a1-a3: barn owl; b1-b3: tawny owl; c1-c3: goshawk. Columns represent repeated trials on the same bird.

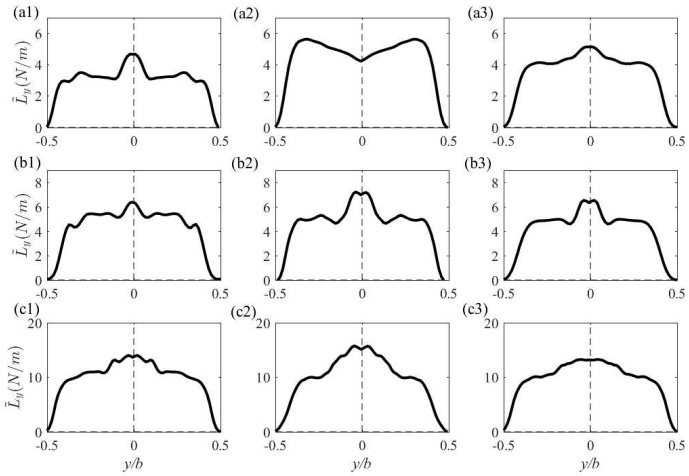

Figure 9: Estimated span loading distributions of nine gliding flights, based on wake measurements using PTV. a1-a3: barn owl; b1-b3: tawny owl; c1-c3: goshawk.

3.4. Limitations

The flights analyzed in this study conflict with the traditional assumptions of the KJG and CMV1/CMV2 models, leading to potential errors in calculating sectional and overall lifts and drags. For the KJG model, the Kutta-Joukowski theorem is certainly applicable to wings, but also blunt bodies such as the bird body/tail region. However, the assumption of 2D flow leads to some error as spanwise flow is obvious around the birds' heads, particularly the blunt head of the barn owl. For the other birds with relatively streamlined heads, the assumption might be more applicable. Further, this model is typically only applicable to relatively small angles of attack when vorticity is only shed from the trailing edge. For our large angle of attack cases, the unsteadiness and likely separation of the flow could lead to large errors. That notwithstanding, Figure 10, which show results for a range of angles of attack, indicates that this model still provides reasonable lift and drag estimates in the barn owl, where the majority of the wing sections are at angles of attack of 20°. Since gliding birds usually exhibit angles less than 20°[36], we consider this model to be broadly applicable to estimate the span loading of most glides, subject to the caveats above.

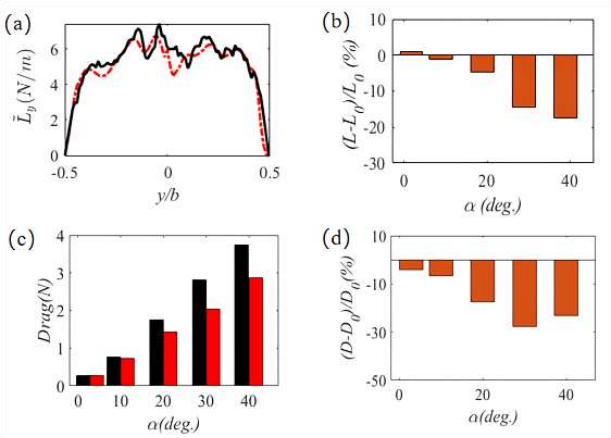

Figure 10: (a) Span loading comparison between the PRS (black line) and KJG (red dash line) with at angles of attack 20° ; (b) Difference in lift estimation of KJG relative to PRS at a range of angles of attack; (c) Drag comparison between the PRS (black bar) and CMV1 (red bar) with five different angles of attack; (d) Difference in lift estimation of CMV1 relative to PRS at a range of angles of attack.

4. CONCLUSIONS

In this study, we use Computational Fluid Dynamics (CFD) modelling to simulate the flow around a high-fidelity barn owl model during free gliding. Using the forces obtained from surface force integration in CFD as a standard, we evaluate the effectiveness of various theoretical models in estimating the aerodynamic performance of gliding flight from simulated flow measurements of the wake. These models successfully predict the lift and spanwise loading, with somewhat less accurate predictions of drag. Our findings suggest that a developed Kutta-Joukowski method that modifies the incoming flow is effective at predicting the lift force and span loading. In comparison, commonly used methods to estimate drag (based on the conservation of momentum in a control volume) predicts the overall drag reasonably well, although its performance at estimating span distribution is less satisfactory. The downstream sampling plane has an effect on results and should be selected carefully for both the lift and drag models, as planes that are too close or too far away will both give substantial errors.

AKNOWLEDGEMENT

This work is supported by the Guangdong Basic and Applied Basic Research Foundation (2023A1515011506), National Natural Science Foundation of China (No. 12302296) and the Guangdong Provincial Key Laboratory of Intelligent Disaster Prevention and Emergency Technologies for Urban Lifeline Engineering (2022B1212010016) to JS, AFOSR European Office for Aerospace Research and Development (FA9550-16-1-0034 to R.J.B. and J.R.U.), the Wellcome Trust (Fellowship-202854/Z/16/Z to J.R.U.).

REFERENCES

1. Gowree, E.R., et al., *Vortices enable the complex aerobatics of peregrine falcons.* Communications Biology, 2018. **1**(1): p. 27.
2. Beratlis, N., et al., *Direct numerical simulations of a great horn owl in flapping flight.* Integrative and Comparative Biology, 2020. **60**(5): p. 1091-1108.
3. Durston, N.E., et al., *Avian surface reconstruction in free flight with application to flight stability analysis of a barn owl and peregrine falcon.* Journal of Experimental Biology, 2019. **222**(9): p. jeb185488.
4. Bomphrey, R.J., et al., *Digital particle image velocimetry measurements of the downwash distribution of a desert locust Schistocerca gregaria.* Journal of the Royal Society Interface, 2006. **3**(7): p. 311-317.
5. Henningsson, P. and A. Hedenström, *Aerodynamics of gliding flight in common swifts.* Journal of Experimental Biology, 2011. **214**(3): p. 382-393.
6. Henningsson, P. and R.J. Bomphrey, *Span efficiency in hawkmoths.* Journal of the Royal Society Interface, 2013. **10**(84): p. 20130099.
7. Henningsson, P., A. Hedenström, and R.J. Bomphrey, *Efficiency of lift production in flapping and gliding flight of swifts.* Plos One, 2014. **9**(2): p. e90170.
8. Spedding, G., *The wake of a kestrel (Falco tinnunculus) in flapping flight.* Journal of Experimental Biology, 1987. **127**(1): p. 59-78.
9. Rosén, M. and A. Hedenström, *Gliding flight in a jackdaw: a wind tunnel study.* Journal of Experimental Biology, 2001. **204**(6): p. 1153-1166.
10. van Dam, C.P., *Accurate prediction of drag using Euler methods.* Journal of Aircraft, 1992. **29**(3): p. 516-519.
11. van Dam, C.P., K. Nikfetrat, and P. Vijgen. *Lift and drag calculations for wings and tails: techniques and applications*. in *Fluid Dynamics in Biology: Proceedings of an AMS-IMS-SIAM Joint Summer Research Conference Held July 6-12, 1991*. 1993. American Mathematical Soc.
12. KleinHeerenbrink, M., K. Warfvinge, and A. Hedenström, *Wake analysis of aerodynamic components for the glide envelope of a jackdaw (Corvus monedula).* Journal of Experimental Biology, 2016. **219**(10): p. 1572-1581.
13. Horstmann, J.T., et al., *Wake development behind paired wings with tip and root trailing vortices: consequences for animal flight force estimates.* PloS One, 2014. **9**(3): p. e91040.
14. Henningsson, P., et al., *The complex aerodynamic footprint of desert locusts revealed by large-volume tomographic particle image velocimetry.* Journal of the Royal Society Interface, 2015. **12**(108): p. 20150119.
15. Bomphrey, R.J., et al., *Tomographic particle image velocimetry of desert locust wakes: instantaneous volumes combine to reveal hidden vortex elements and rapid wake deformation.* Journal of the Royal Society Interface, 2012. **9**(77): p. 3378-3386.
16. Houghton, E., et al., *Aerodynamics for Engineering Students. 7th*. 2017, Elsevier.
17. Pennycuick, C., et al., *The profile drag of a hawk's wing, measured by wake sampling in a wind tunnel.* Journal of Experimental Biology, 1992. **165**(1): p. 1-19.
18. Klaassen van Oorschot, B., E.A. Mistick, and B.W. Tobalske, *Aerodynamic consequences of wing morphing during emulated take-off and gliding in birds.* Journal of Experimental Biology, 2016. **219**(19): p. 3146-3154.
19. Tucker, V.A., *Gliding birds: the effect of variable wing span.* Journal of Experimental Biology, 1987. **133**(1): p. 33-58.
20. KleinHeerenbrink, M. and A. Hedenström, *Wake analysis of drag components in gliding flight of a jackdaw (Corvus monedula) during moult.* Interface Focus, 2017. **7**(1): p. 20160081.
21. Pennycuick, C., et al., *Wingbeat frequency and the body drag anomaly: wind-tunnel observations on a thrush nightingale (Luscinia luscinia) and a teal (Anas crecca).* Journal of Experimental Biology, 1996. **199**(12): p. 2757-2765.
22. Hedenström, A. and F. Liechti, *Field estimates of body drag coefficient on the basis of dives in passerine birds.* Journal of Experimental Biology, 2001. **204**(6): p. 1167-1175.
23. Pennycuick, C.J., *Bird flight performance: a practical calculation manual*. 1989: Oxford University Press.
24. Henningsson, P. and R.J. Bomphrey, *Time-varying span efficiency through the wingbeat of*

desert locusts. Journal of the Royal Society Interface, 2012. **9**(71): p. 1177-1186.
25. GR Spedding, J.M., *Span efficiencies of wings at low Reynolds numbers.* Journal of Aircraft, 2010. **47**(1): p. 120-128.
26. Anderson, J., *Fundamentals of aerodynamics, Forth Edittion*. 2010: Tata McGraw-Hill Education.
27. van Dam, C., et al., *Drag prediction at subsonic and transonic speeds using Euler methods.* Journal of Aircraft, 1995. **32**(4): p. 839-845.
28. van Dam, C.P., *Recent experience with different methods of drag prediction.* Progress in Aerospace Sciences, 1999. **35**(8): p. 751-798.
29. Katz, J. and A. Plotkin, *Low-speed aerodynamics*. Vol. 13. 2001: Cambridge university press.
30. Bai, C. and Z. Wu, *Generalized Kutta–Joukowski theorem for multi-vortex and multi-airfoil flow (a lumped vortex model).* Chinese Journal of Aeronautics, 2014. **27**(1): p. 34-39.
31. Usherwood, J.R. and C.P. Ellington, *The aerodynamics of revolving wings I. Model hawkmoth wings.* Journal of Experimental biology, 2002. **205**(11): p. 1547-1564.
32. Spedding, G., *The wake of a kestrel (Falco tinnunculus) in gliding flight.* Journal of Experimental Biology, 1987. **1**(1): p. 45-57.
33. Cheney, J.A., et al., *From wing shape to fluid dynamics in the barn owl (Tyto alba).* BioRxiv, 2020: p. 2020.05. 29.121178.
34. Usherwood, J.R., et al., *High aerodynamic lift from the tail reduces drag in gliding raptors.* Journal of Experimental Biology, 2020. **223**(3): p. jeb214809.
35. Song, J., et al., *Virtual manipulation of tail postures of a gliding barn owl (Tyto alba) demonstrates drag minimization when gliding.* Journal of the Royal Society Interface, 2022. **19**(187): p. 20210710.
36. Cheney, J.A., et al., *Raptor wing morphing with flight speed.* Journal of the Royal Society Interface, 2021. **18**(180): p. 20210349.